

Quantifying the Performance of Flexible Propulsors with Nonuniform Stiffness

Hakeem Frank

Xavier University of Louisiana

Monica Kala

Tulane University

Griffin Sandler

Tulane University

July 2, 2016

Abstract

In order to mimic the motion of the flexible appendages of various species, we model flexible panels using spring forces and beam forces. By incorporating the immersed boundary method, we were able to heave both panel with a background velocity. We vary panel rigidity and heaving frequency of panels with uniform and nonuniform beam stiffness composition and record their thrust output and deflection. We associate each panel rigidity and frequency with the dimensionless value Π_i representing effective flexibility. By plotting our data, we investigate the relationship between effective flexibility and thrust output for uniform panels. Local maxima in thrust output correspond with specific effective flexibilities across various beam stiffnesses and frequencies. Similarly, when heaved, panels with nonuniform stiffnesses output a higher thrust than those with uniform stiffness of the same values. Beam mode analysis is used to relate effective flexibility to trailing edge amplitude which corresponds to optimized thrust output.

1 Introduction

Animals that move through air or water do so by accelerating the fluid around them. Acceleration of those fluids occurs by movement of the animals' flexible appendages. These animal propulsors are the generally replicated in engineering applications by some rigid heaving structure with the goal of generating movement. However, the wing of an eagle is much more flexible than the wing of a Boeing 747, and in general, these animal propulsors are much more flexible than those other propulsors. Understanding how flexible propulsors accelerate fluid will be useful for future engineering endeavors.

Recent studies have investigated the kinematics of these swimming and flying animals. Similarities between these types of animals have been discovered, and a wide variety of animal sizes, fluid mediums, and species shared the same range of animal bending kinematics. Not only were the bending patterns similar but those similar bending patterns were limited to a few fundamental design characteristics [3].

A flexible propulsor is usually modeled for study by creating a panel with uniform stiffness that is heaved up and down in a fluid with a background flow. Although most

propulsors are modeled using panels of uniform stiffness, panels of nonuniform stiffness are found to create a more accurate model of the swimming performance of the flexible propulsors of fish [4].

Recent work has shown that the propulsive performance of heaving flexible panels depends on the structural resonance of the panel [8]. This structural resonance is determined by the effective flexibility of the panel. The effective flexibility is a dimensionless number that describes the ratio of added mass forces to internal bending stresses, and is dependent on the heaving frequency of the panel and the flexural rigidity of the panel. The same study found that trailing edge amplitude and thrust had local maximas at specific effective flexibility values. These effective flexibility were found to correspond with dominant eigenmodes to the Euler Bernoulli beam equation.

2 Goals

We will confirm the results of previous papers by comparing the thrust output and effective flexibility of our panels model. In addition, we will investigate the difference in thrust output between panels of uniform stiffness and nonuniform stiffness. Finally, we will perform the beam mode analysis using the one end fixed, one end free form of the Euler Bernoulli beam equation on panels with uniform stiffness to further confirm the results of previous experiments with the eventual goal of using a modified beam equation to analyze panels of nonuniform stiffnesses. To accomplish these goals, we will first model the flexible properties of propulsors by varying the flexural rigidity of heaving uniform stiffness panels. We will then simulate a fluid flow around the panels using the immersed boundary method. In our simulations, we will record a variety of outputs including thrust, deflection, and trailing edge amplitude.

3 Euler-Bernoulli Beam Equation

In the graphical representation of the beam shown in Figure 1, heaving movements occur in the y -direction, while the length of the beam is represented from 0 to L in the x -direction. We begin with the equation of dynamic equilibrium condition for forces in the y -direction, represented as the sum of the forces above:

$$V - (V + \frac{\partial V}{\partial x}dx) - \rho A dx \frac{\partial^2 v}{\partial t^2} = 0 \quad (1)$$

where V is the shearing force applied to the beam, A is the area of the cross section, ρ is the density of the beam, and v is the deflection of the beam. Equation 1 describes the forces of the beam at equilibrium. We can rewrite the equation as

$$\frac{\partial V}{\partial x}dx = -\rho A dx \frac{\partial^2 v}{\partial t^2} \quad (2)$$

We introduce the bending moment equilibrium condition:

$$-Vdx + \frac{\partial M}{\partial x}dx = 0, \quad (3)$$

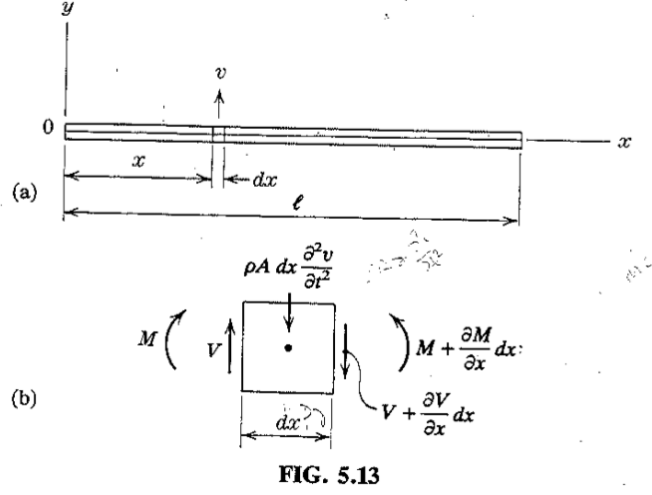


FIG. 5.13

[9]

Figure 1: Diagram of a beam

where M is the bending moment of the beam. If we solve for Vdx and substitute Equation 3 into Equation 2, we get

$$\frac{\partial^2 M}{\partial x^2} dx = -\rho A dx \frac{\partial^2 v}{\partial t^2} \quad (4)$$

We're given the relationship

$$M = EI \frac{\partial^2 v}{\partial x^2}, \quad (5)$$

where EI is flexural rigidity, which is constant in the case of a prismatic beam.

Plugging in our equation for M in Equation 4, we arrive at the homogeneous version of the Euler-Bernoulli Beam Equation

$$EI \frac{\partial^4 v}{\partial x^4} + \rho A \frac{\partial^2 v}{\partial t^2} = 0. \quad (6)$$

To model the motion of a beam with length L , width W , and height δ in a fluid, we let $A = \delta W$, and specify ρ_p as the density of the beam, while setting the equation equal to an external force, F_{ext}

$$EI \frac{\partial^4 v}{\partial x^4} + \rho_p \delta W \frac{\partial^2 v}{\partial t^2} = F_{ext}. \quad (7)$$

In our case, an external force would be drag from the fluid.

3.1 Non-Dimensionalization of the Beam Equation

We now non-dimensionalize the Euler Bernoulli Beam Equation to separate the inertial forces from the bending forces. To begin, consider the Euler-Bernoulli Beam Equation, labeled as Equation 7. Since added mass forces will dominate over inertial forces on the panel, $\rho_p \delta W$ can be rewritten as $\rho L W$. Additionally, substituting in dimensionless variables of $x^* = \frac{x}{L}$, $t^* = t\omega$, and $v^* = \frac{v}{a'}$ into the beam equation yields the following equation:

$$\frac{\partial^4 v^* a'}{\partial (x^* L)^4} + \rho L W \frac{\partial^2 v^* a'}{\partial (t^* \omega^{-1})^2} = F_{ext}^* E I a' L^{-4},$$

where a' is the trailing-edge amplitude of the beam and ω is the heaving frequency. Simplifying the equation, we obtain

$$\frac{\partial^4 v^*}{\partial (x^*)^4} + \rho L^5 W E I^{-1} \omega^2 \frac{\partial^2 v^*}{\partial (t^*)^2} = F_{ext}^*. \quad (8)$$

Setting

$$\Pi = \sqrt{\rho L^5 W E I^{-1} \omega^2} \quad (9)$$

and substituting Π^2 into the Beam Equation

$$\frac{\partial^4 v^*}{\partial (x^*)^4} + \Pi^2 \frac{\partial^2 v^*}{\partial (t^*)^2} = F_{ext}^* \quad (10)$$

The Euler-Bernoulli Beam Equation now has been transformed into a non-dimensional equation. With the introduction of the effective flexibility Π , we are able to characterize the ratio of added mass forces and internal bending forces.

3.2 Solving for the Euler-Bernoulli Beam Equation

We would now like to solve the non-dimensionalized Euler-Bernoulli beam equation. For simplification, we assume that our variables are non-dimensionalized. We consider the homogeneous case for the Euler-Bernoulli beam equation, such that $F_{ext} = 0$:

$$\frac{\partial^4 v}{\partial x^4} + \Pi^2 \frac{\partial^2 v}{\partial t^2} = 0 \quad (11)$$

When a beam vibrates transversely in one of its natural modes, the deflection $v(x, t)$ at any time can be measured using the following equation:

$$v(x, t) = X(A \cos(\omega t) + B \sin(\omega t)) \quad (12)$$

The equation for v appears to be the product of two functions, $X(x)$ and $T(t)$, where T is a temporal function of time t , and X is a spatial function of the distance x from the left-hand side of the beam. Thus we can rewrite v as

$$v = X(x)T(t)$$

Substituting v into equation (12) and simplifying yields the equation:

$$\frac{\partial^4 X}{\partial x^4} T - \Pi^2 \omega^2 T X = 0 \quad (13)$$

To help us solve the homogeneous, fourth order differential equation above, let $k^4 = \Pi^2 \omega^2$.

Therefore,

$$\frac{\partial^4 X}{\partial x^4} - k^4 X = 0.$$

If we let $X = e^{nx}$, we obtain

$$e^{nx}(n^4 - k^4) = 0$$

Solving for n , we have four solutions for n : $n_1 = k, n_2 = -k, n_3 = ik, n_4 = -ik$, where $i = \sqrt{-1}$. Thus, the general solution of our fourth order differential equation is

$$X = Ae^{kx} + Be^{-kx} + Ce^{ikx} + De^{-ikx}$$

Which, for our purposes, we can rewrite as

$$\begin{aligned} X = & C_1(\cos(kx) + \cosh(kx)) + C_2(\cos(kx) - \cosh(kx)) \\ & + C_3(\sin(kx) + \sinh(kx)) + C_4(\sin(kx) - \sinh(kx)) \end{aligned}$$

Since we are investigating the behavior of beams with one end fixed and one end free, we will use the boundary conditions:

$$(X)_{x=0} = 0 \quad \left(\frac{dX}{dx}\right)_{x=0} = 0 \quad \left(\frac{d^2X}{dx^2}\right)_{x=L} = 0 \quad \left(\frac{d^3X}{dx^3}\right)_{x=L} = 0$$

These conditions describe the beam's boundaries; at the leading edge of the beam ($x = 0$), the displacement X is fixed and is thus zero. The slope at the leading edge also maintains a flat shape, characteristic of a clamped leading edge. The concavity at the trailing edge of the beam is zero, and thus the change in concavity is also zero.

From the first two conditions, we notice that $C_1 = 0$ and $C_3 = 0$. We continue solving for our remaining coefficients C_2 and C_4 by taking the second derivative of X with respect to x :

$$\frac{d^2X}{dx^2} = k^2[C_2(-\cos(kx) - \cosh(kx)) + C_4(-\sin(kx) - \sinh(kx))]$$

We then evaluate $\frac{d^2X}{dx^2}$ at $x = L$ in order to solve for C_2 :

$$\begin{aligned} 0 = & C_2(\cos(kL) + \cosh(kL)) + C_4(\sin(kL) + \sinh(kL)) \\ C_2 = & -C_4 \frac{\sin(kL) + \sinh(kL)}{\cos(kL) + \cosh(kL)} \end{aligned}$$

By evaluating $\left. \frac{d^3 X(x)}{dx^3} \right|_{x=L}$ we are able to solve the equation for our remaining coefficient, C_4 :

$$\begin{aligned} \frac{d^3 X(L)}{dx^3} &= k^3 [C_2(\sin(kL) - \sinh(kL)) + C_4(-\cos(kL) - \cosh(kL))] = 0 \\ 0 &= C_2(\sin(kL) - \sinh(kL)) + C_4(-\cos(kL) - \cosh(kL)) \end{aligned}$$

We plug C_2 into our equation and solve for C_4 :

$$\begin{aligned} 0 &= (-C_4 \frac{\sin(kL) + \sinh(kL)}{\cos(kL) + \cosh(kL)})(\sin(kL) - \sinh(kL)) - C_4(\cos(kL) + \cosh(kL)) \\ 0 &= C_4(\frac{\sin^2(kL) - \sinh^2(kL)}{\cos(kL) + \cosh(kL)} + \cos(kL) + \cosh(kL)) \\ 0 &= C_4(\sin^2(kL) - \sinh^2(kL) + \cos^2(kL) + 2\cosh(kL)\cos(kL) + \cosh^2(kL)) \\ 0 &= C_4(2 + 2\cosh(kL)\cos(kL)) \\ -C_4 &= C_4\cosh(kL)\cos(kL) \\ -1 &= \cosh(kL)\cos(kL) \end{aligned}$$

We note that attempting to solve for C_4 using C_2 leads us to the frequency equation

$$-1 = \cosh(kL)\cos(kL) \tag{14}$$

Therefore, the values for each of the four weights in X are:

$$C_1 = 0 \quad C_2 = -C_4 \frac{\sin(kL) + \sinh(kL)}{\cos(kL) + \cosh(kL)} \quad C_3 = 0 \quad C_4 = s, \forall s \in R$$

3.3 Solving for k Using Newton's Method

To get closer to a numeric value for C_2 , we use Newton's method to find the roots of $-1 = \cosh(kL)\cos(kL)$.

We begin by guessing an approximate solution $k^i L$ of $-1 = \cosh(kL)\cos(kL)$, and then we plug it into the formula:

$$k^{i+1}L = k^iL - \frac{f(k^iL)}{f'(k^iL)}$$

Note that this is the formula for Newton's method, where $k^i L$ is our current guess, and $k^{i+1}L$ is the next estimate for finding a root. We created an algorithm in Matlab that allows us to find a root using an initial estimate. The program iterates the function until $k^{i+1}L - k^iL < 1 \times 10^{-9}$.

We found 4 roots using Newton's method in Matlab:

$$k_1L = 1.875 \quad k_2L = 4.694 \quad k_3L = 7.855 \quad k_4L = 10.996$$

3.4 Calculating Eigenmodes

With these solutions, we can approximate k for our X function by dividing each root by a given length. We now have an equation for the transverse vibrations of a prismatic beam, dependent on C_4 :

$$X_j = C_4 \left(-\frac{\sin(k_j L) + \sinh(k_j L)}{\cos(k_j L) + \cosh(k_j L)} (\cos(k_j x) - \cosh(k_j x)) + (\sin(k_j x) - \sinh(k_j x)) \right)$$

If we let $C_4 = 1$, then we have the spatial solution

$$\phi_j = -\frac{\sin(k_j L) + \sinh(k_j L)}{\cos(k_j L) + \cosh(k_j L)} (\cos(k_j x) - \cosh(k_j x)) + (\sin(k_j x) - \sinh(k_j x))$$

We now see that the vibrations of a prismatic beam can be decomposed to the sum of infinite eigenmodes, all of which have a modal contribution dependent on t :

$$v(x, t) = \sum_{j=1}^{\infty} \phi_j(x) C_i(t).$$

In order to accurately see the effects of each modal contribution, we normalize ϕ_j to negate the scaling effect from C_4 .

To normalize ϕ_j , we set $\hat{\phi}_j = \frac{\phi_j}{\sqrt{\langle \phi_j, \phi_j \rangle}}$

Thus, the solution to the Euler-Bernoulli beam equation represents the deflection in terms of displacement functions $\hat{\phi}$ and time functions $C_i(t^*)$:

$$v(x, t) = \sum_{j=1}^{\infty} \hat{\phi}_j(x) C_j(t) \quad (15)$$

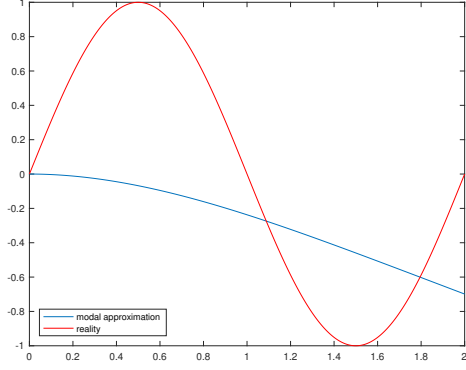
where ϕ_i are orthonormal eigenfunctions and C_j are the modal contributions of each eigenfunction, which is calculated using the experimental deflection, v_{exp} :

$$C_j(t) = \int_0^L v_{exp}(x, t) \hat{\phi}_j(x) dx$$

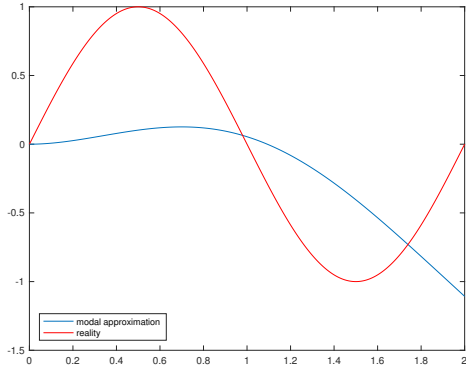
Finally, we are able to use $v(x, t)$ to analyze the modal decomposition of an experimental deflection. We did so with four values of k_j , $L = .025$, and $v_{exp} = \sin(\phi x)$

4 Forces

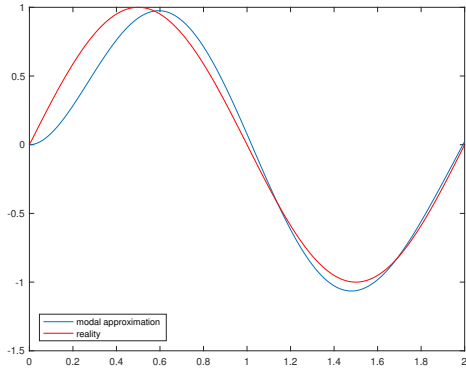
Our goal is to create a model of a panel of N_x by N_y nodes that resists compression and elongation due to spring forces and maintains a specific shape due to beam forces. Then we add incorporate target forces in order to heave the panel's leading edge to a desired location. We will then place this entire system into a fluid with flow and measure the amplitude of the panel's trailing edge in order to see the relationship between panel flexibility and thrust. The following sections outline the specifics with which we incorporate each force component.



(a) Modal Approximation with $\hat{\phi}_1 C_1$



(b) Modal Approximation with $\hat{\phi}_1 C_1 + \hat{\phi}_2 C_2$



(c) Modal Approximation with $\hat{\phi}_1 C_1 + \hat{\phi}_2 C_2 + \hat{\phi}_3 C_3$

Figure 2: Modal Approximations for a Sine Function

4.1 Spring Forces

A spring is an object that can be elongated or compressed by a force. However, when the force is removed, a spring will return to its original length. We can model the movement of springs using Hooke's Law. Hooke's Law states that the force required to move a spring is directly proportional to the length of deformation. It is written as $F_s = k_s x$ where F_s represents the spring force, k_s the spring constant, and x is the distance from the resting length.

In Figure 3, x represents the distance of a point of mass m from its resting length (equilibrium). Here we see that the point acts as a spring. When it is compressed, F_s is greater than 0 meaning the point would like to stretch to reach its equilibrium position. Meanwhile, when it is elongated, F_s is less than 0 causing the point to want to compress to reach its equilibrium position.

We model the behavior of this specific point using a the spring mass-damper equation:

$$m \frac{\partial^2 x}{\partial t^2} + D \frac{\partial x}{\partial t} + k_s x = 0 \quad (16)$$

where

- m is the point mass in our case equivalent to 1
- D is damping coefficient
- k_s is the spring constant
- x is the distance from resting length

The damping coefficient characterizes how quickly the point returns to its equilibrium solution. The stronger the damping parameter, the fewer oscillations the spring will undergo, and the quicker it will return to its original length. We then expand on this equation in order to encompass a series of springs within a network and apply our knowledge of spring behavior to a network of nodes connected by springs. The forces within the entire panel are found using a modification of the spring mass damper equation:

$$m \frac{\partial^2 \vec{X}}{\partial t^2} + D \frac{\partial \vec{X}}{\partial t} + \vec{f}_s(\vec{X}) = 0 \quad (17)$$

where

- $\vec{X} = (X, Y)$ are the spatial coordinates of a point on the structure
- $\vec{f}_s(\vec{X})$ are the spring forces at point \vec{X}

For a continuous structure in the material coordinate frame q , we derive the spring forces and incorporate them into Equation 17.

$$\begin{aligned}\vec{f}_s(\vec{X}(q, t)) &= \frac{\partial}{\partial q} T \tau \\ \tau &= \frac{\frac{\partial \vec{X}}{\partial q}}{\left| \frac{\partial \vec{X}}{\partial q} \right|} \\ T &= k_s \left(\left| \frac{\partial \vec{X}}{\partial q} \right| - 1 \right)\end{aligned}$$

- T is the tension of the spring (due to Hooke's Law)
- τ is the unit tangent vector of the fiber
- k_s is the spring stiffness of the filament

We create and model this system in Matlab. Figure 4 provides an example of a network where N_x and N_y equal 4. The nodes are represented by black asterisks while the springs are shown as colored lines. Each node in this system is at rest at its equilibrium position, and all springs in this system have the same spring constant k_s .

When a node is moved from its initial position the nodes reacts appropriately as each moves to its equilibrium location. In Figure 5, the first image shows the initial perturbation. The first node is moved to half of its resting length. In the second image, we see that every node in the panel is shifting to adjust for this initial perturbation as expected. Each spring stretches or compresses in order to reach its resting length. In the final image, each spring has returned to its resting length and is in equilibrium. Therefore, there will be no further movement. The damping coefficient in this case (recall Equation 17) is 0.5. This allows for the spring panel to return to its resting length.

4.2 Incorporating Beam Forces

Now we incorporate horizontal beams into our network. First we distinguish between spring and beam forces in order to avoid confusion.

In the material coordinate frame q , we characterize both spring and beam forces simply. Figure 6 exhibits the difference between spring and beam forces. Beam forces are elastic forces that move to maintain a specific shape. They incorporate a beam constant as seen in Equation 18. While spring forces are applied in the direction of our nodes, beam forces are applied in a perpendicular manner. Both are important in maintaining the validity of our panel as spring forces allow for the resistance of shortening and lengthening of our panel and beam forces prevent a large distortion of shape.

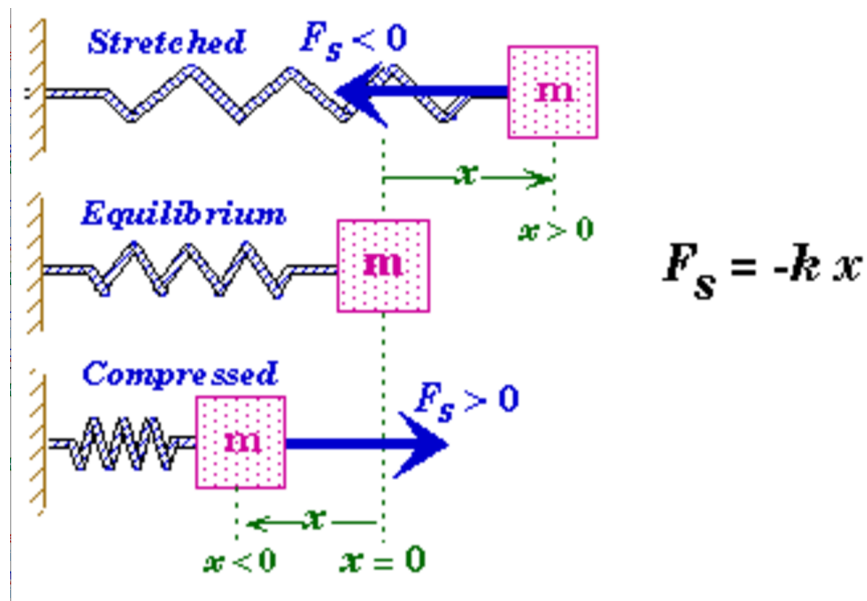


Figure 3: Example of Hooke's law

photo from umn.edu

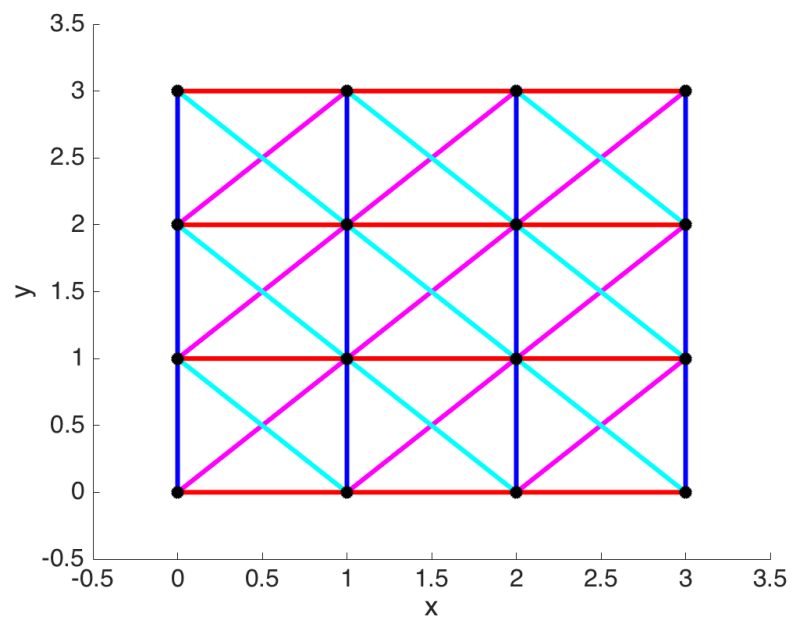
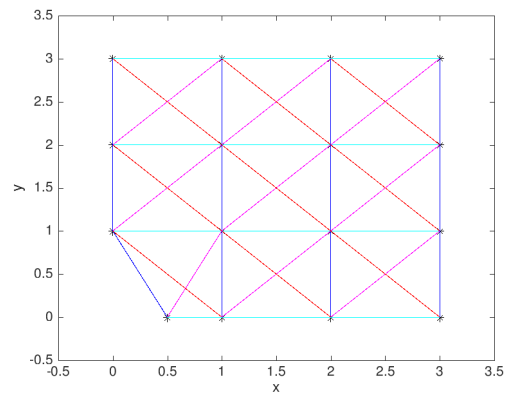
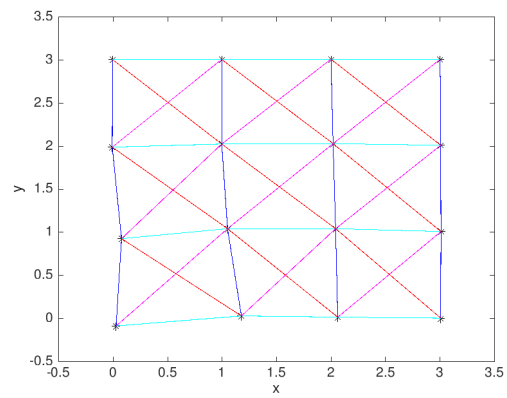


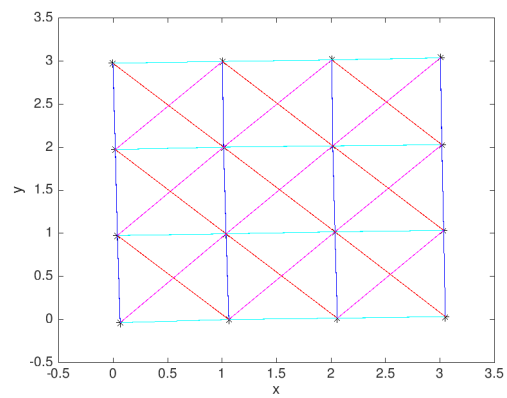
Figure 4: 4x4 Panel at Rest



(a)



(b)



(c)

Figure 5: Panel Perturbed Reaction

We see that it is possible for us to modify our spring-mass damper network in order to incorporate beam forces.

We can call this the spring-beam-mass damper network.

$$m \frac{\partial^2 \vec{X}}{\partial t^2} + D \frac{\partial \vec{X}}{\partial t} + \vec{f}_s(\vec{X}) + \vec{f}_b(\vec{X}) = 0 \quad (18)$$

where

- $\vec{f}_b(\vec{X})$ are the beam forces at \vec{X} based on its desired shape

We can derive the beam forces and incorporate them into Equation 18.

$$\vec{f}_b(\vec{X}(q, t)) = \frac{\partial^2}{\partial q^2} \left(k_b \frac{\partial^2 \vec{X}}{\partial q^2} \right)$$

where

- k_b is the beam stiffness (or flexural rigidity) of the filament

We incorporate beam forces into the horizontal nodes of the network in groups of three where the force acts on the middle node as in Figure 6. Therefore, we now have spring forces between all surrounding nodes and beam forces within the horizontal nodes. In Figure 7, the pink, cyan, and blue lines represent the springs of the network while the beams are circled in black. They are selected in groups of 3 nodes.

4.3 Incorporating Target Forces

We heave the leading edge of the structure by applying an external force proportional to the distance between the structure's current location and the desired location.

Equation 18 can be modified to include these forces known as target forces. Equation 19 incorporates all three forces known thus far to create a spring-beam-target damper network.

$$m \frac{\partial^2 \vec{X}}{\partial t^2} + D \frac{\partial \vec{X}}{\partial t} + \vec{f}_s(\vec{X}) + \vec{f}_b(\vec{X}) + \vec{f}_t(\vec{X}) = 0 \quad (19)$$

where

- $\vec{f}_s(\vec{X})$ are the spring forces
- $\vec{f}_b(\vec{X})$ are the beam forces
- $\vec{f}_t(\vec{X})$ are the target forces

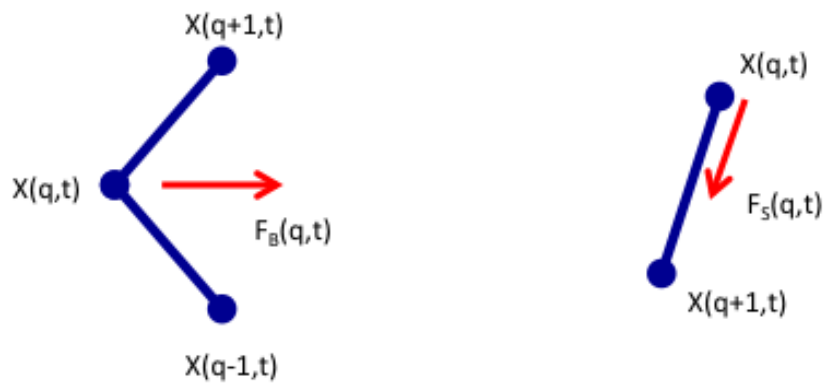


Figure 6: Beam and Spring Forces

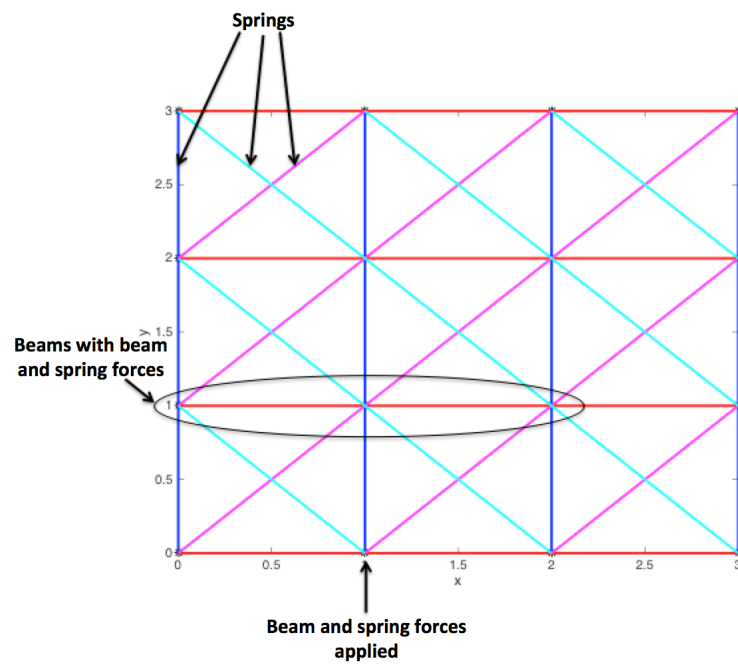


Figure 7: Beam and Spring Network

We can find $\vec{f}_t(\vec{X})$ using Equation 20 below.

$$\vec{f}_t(\vec{X}) = k_t(\vec{X}^* - \vec{X}) \quad (20)$$

where

- k_t is the target force spring constant
- $\vec{X}(q, t)$ is the current location of our point
- $\vec{X}^*(q, t)$ is the desired location of point

Target forces are applied at the leading edge of the network as shown in Figure 8

In Figure 9, we have a set of images demonstrating a panel with both beam and spring forces heaving over time. We see how the beam forces attempt to keep the panel in the shape of a line while the spring forces are allowing the panel to resist elongation and compression.

Thus far we have been incorporating a damping force D as seen in Equation 19. We've been using this parameter to act as a substitution for the effects of fluid on the panel. Next, we remove the damping force and instead incorporate a background velocity as a fluid. This is done in the next section.

5 Navier-Stokes Equation

In order to model the movement of a heaving flexible panel in fluid, we incorporate equations of fluid motion into our simulation. The equations that account for fluid motion are the Navier-Stokes equations for viscous, incompressible fluid flow. By numerically solving for the Navier-Stokes equations, we are able to compute the velocity of fluid elements surrounding our beam. This is necessary in simulating the interaction of the beam with the surrounding fluid, accomplished using the Immersed Boundary Method, which we discuss in the subsequent sections.

We begin by remarking that fluid flows will be represented in an Eulerian coordinate system, rather than in a Lagrangian coordinate system. The difference between the two is that in the Eulerian coordinate system, points are fixed in space, and fluid properties are monitored as functions of time as the flow passes those fixed spatial locations. In the Lagrangian reference frame, fluid particles are followed throughout different locations in the fluid domain. It is conventional to use the Eulerian view of fluid motion, because velocity can be measured directly at each fixed spatial coordinate, rather than calculated as the time-rate of change of a fluid particle location moving through the fluid.

The Navier-Stokes equations are derived from the equations for conservation of mass and conservation of momentum [5]. However, rather than viewing the equation for the conservation of momentum with point masses, we consider the time rate of change of momentum of a fluid element, or $\frac{\partial u}{\partial t}$. In addition to the local acceleration of a fluid element, we also consider the convective acceleration $(u \cdot \nabla)u$, which accounts for force exerted on a particle

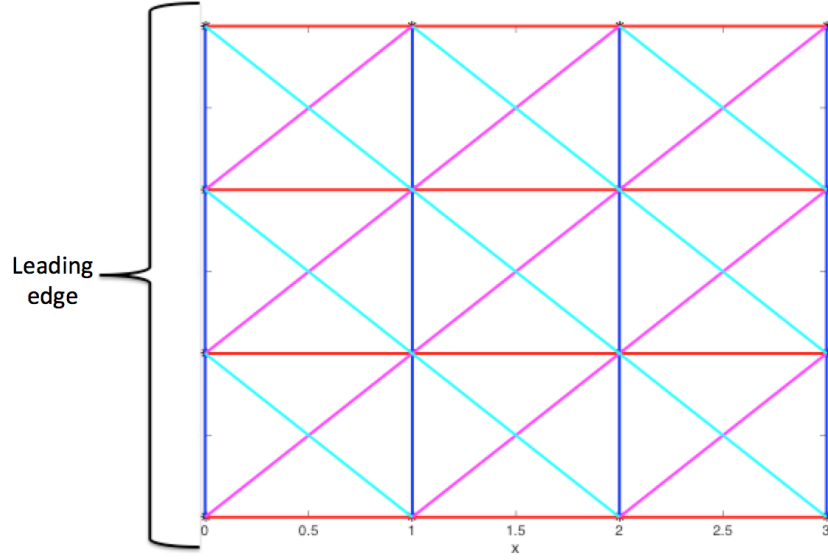


Figure 8: Leading Edge

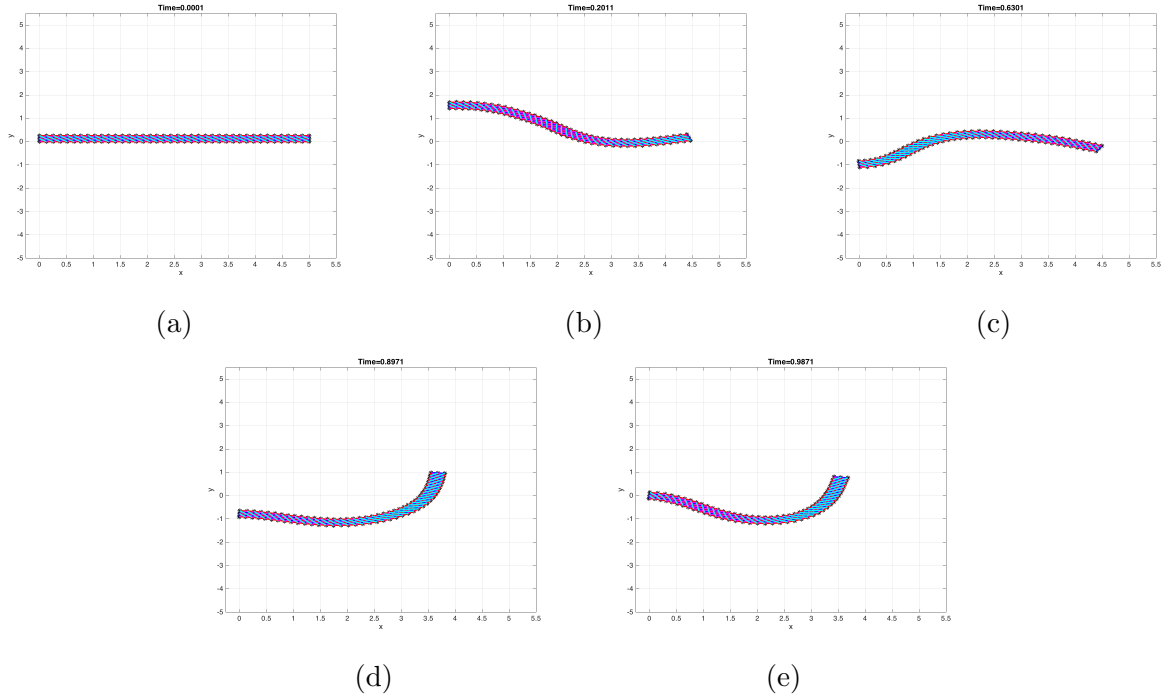


Figure 9: Heaving Panel with Target Forces

of fluid by the other particles of fluid surrounding it. This is how the fluid accelerates in a non-uniform flow. We derive these acceleration components using the substantial derivative of fluid velocity:

$$\frac{Du}{Dt} = \frac{\partial u}{\partial t} + (u \cdot \nabla)u$$

The substantial derivative allows us to describe Lagrangian acceleration in an Eulerian reference frame. The forces represented in the Navier-Stokes equations are pressure forces from the fluid, viscous forces within the fluid, and additional body-forces, which in our case are the forces associated with the beam.

Thus, the form of the Navier-Stokes Equations as a fluid version of the equation of conservation of momentum is:

$$\rho \left(\frac{\partial u}{\partial t} + (u \cdot \nabla)u \right) = -\nabla p + \mu \Delta u + f(x, t) \quad (21)$$

where ρ is density, u is the fluid velocity, p is pressure, μ is the dynamic viscosity, and $f(x, t)$ are external forces acting on the fluid. The left-hand side of the equation represents the inertial terms, and the right-hand side of the equation represents the sum of pressure forces ∇p , viscous forces $\mu \Delta u$, and body-forces $f(x, t)$. We assume incompressibility of the fluid, and thus the conservation of mass implies that

$$\nabla \cdot u = 0 \quad (22)$$

Together, Equations 21 and 22 constitute the Navier-Stokes Equations of incompressible flow.

At this point, we non-dimensionalize the Navier-Stokes equations to identify dimensionless parameters that characterize the behavior of the solutions of the Navier-Stokes equations. By non-dimensionalizing the Navier-Stokes equations, we determine the Reynolds Number, which gives insight into the ratio of inertial forces of the object to the viscous forces of the fluid.

To begin we start with the dimensional Navier-Stokes Equation:

$$\rho \left(\frac{\partial u}{\partial t} + (u \cdot \nabla)u \right) = -\nabla p + \mu \Delta u \quad (23)$$

with no external forces.

To non-dimensionalize Equation 23 we introduced non-dimensional parameters related to the parameters listed above. Let $X' = \frac{x}{L}$ where x is the position of the fluid and L is the characteristic length, $t' = \frac{t}{T} = \frac{t}{\frac{L}{u}}$ where u is the characteristic velocity, $\nabla' = L \cdot \nabla$, $\Delta' = L^2 \cdot \Delta$, $p' = \frac{p}{\rho u^2}$.

After performing the desired substitutions our new Navier-Stokes Equation is

$$\rho(u(\frac{u}{L} \frac{\partial u'}{\partial t'} + u^2(L^{-1})(u \cdot \nabla)u) = (L^{-1})(\rho u^2)(-\nabla' p') + (L^{-2})(u \mu \Delta' u') \quad (24)$$

After combining and canceling terms

$$\left(\frac{\partial u'}{\partial t'} + (u \cdot \nabla)u\right) = (-\nabla' p') + L^{-1}U^{-1}\rho^{-1}\mu(\Delta' u') \quad (25)$$

Recognizing that

$$L^{-1}U^{-1}\rho^{-1}\mu = \frac{1}{Re} \quad (26)$$

where Re is the Reynolds Number

Our final form of the Non-dimensional Navier-Stokes Equation is

$$\left(\frac{\partial u'}{\partial t'} + (u' \cdot \nabla')u'\right) = (-\nabla' p') + \frac{1}{Re}(\Delta' u') \quad (27)$$

We have determined the relationship between internal forces and viscous forces acting of the fluid and are able to incorporate the fluid flow in our panel system.

6 Immersed Boundary Method

As mentioned previously, numerically solving for the Navier-Stokes equations is a necessary step in the process that we use to model the interaction between our heaving panel and a surrounding fluid, known as the Immersed Boundary Method[7]. We think of our model as a fluid structure interaction problem and consider the panel as an elastic boundary that interacts with a background flow. The boundaries forces impact the fluid forces, and the fluid velocity impacts the velocity and position of the boundary. It is necessary to consider the fluid domain on an Eulerian grid with fixed, square domain of length Ω . After we determine our grid spacing, $Ngrid$, we calculate the distance between grid points as $dx = \Omega/Ngrid$. We then consider the boundary on a Lagrangian mesh, Γ , with a fixed length, S_L , and fixed width, S_W . If we want the two Lagrangian points to be between each Eulerian grid space, we calculate the number of nodes needed to make the length and width to be $NS_L = \text{ceil}(S_L/(.5dx))$ and $NS_W = \text{ceil}(S_W/(.5dx))$. We calculate the distance between each Lagrangian point to be $ds_L = S_L/(NS_L - 1)$, in the x direction and $ds_W = S_W/(NS_L - 1)$, in the y direction. The equations of motion of the system are:

$$\rho \left(\frac{\partial \mathbf{u}(\mathbf{x}, t)}{\partial t} + \mathbf{u}(\mathbf{x}, t) \cdot \nabla \mathbf{u}(\mathbf{x}, t) \right) = -\nabla p(\mathbf{x}, t) + \mu \Delta \mathbf{u}(\mathbf{x}, t) + \mathbf{f}(\mathbf{x}, t) \quad (28)$$

$$\nabla \cdot \mathbf{u} = 0 \quad (29)$$

$$\mathbf{f} = \int_{\Gamma} \mathbf{F}(q, t) \delta(\mathbf{x} - \mathbf{X}(q, t)) dq \quad (30)$$

$$\mathbf{U}(q, t) = \frac{\partial \mathbf{X}(q, t)}{\partial t} = \int_{\Omega} \mathbf{u}(\mathbf{x}, t) \delta(\mathbf{x} - \mathbf{X}(q, t)) d\mathbf{x} \quad (31)$$

$$\mathbf{F}(q, t) = F[\mathbf{X}(\cdot, t); q, t] \quad (32)$$

where $x = (x, y, z)$, $u(x, t) = (u_1(x, t), u_2(x, t))$ is the fluid velocity and $p(x, t)$ is the fluid pressure. Here, Equations 28 and 29 are the Navier-Stokes Equations, Equation 30 calculates the external force acting on the fluid, Equation 31 interpolates the velocity and position of the Lagrangian points on the Eulerian grid, and Equation 32 calculates the elastic forces of the panel.

The Immersed Boundary Method uses a $\delta_h(x)$ to approximate impact of the translation between the fluid and the boundary. Let

$$\delta_h(x) = h^{-2} \Phi\left(\frac{x_1}{h}\right) \Phi\left(\frac{x_2}{h}\right) \quad (33)$$

where $x = (x_1, x_2)$, h is the mesh width and where Φ is uniquely defined by:

- (i) Φ is a continuous function
- (ii) $\Phi(r) = 0$ for $r \geq 2$.
- (iii) For all r ,

$$\sum_{j \text{ even}} \Phi(r - j) = \sum_{j \text{ odd}} \Phi(r - j) = \frac{1}{2} \quad (33)$$

- (iv) For all r ,

$$\sum_j (r - j) \Phi(r - j) = 0; \quad (33)$$

- (v) For all r ,

$$\sum_j (\Phi(r - j))^2 = C, \quad (33)$$

where C is independent of r .

These five conditions uniquely define the function Φ , including the constant, C , and therefore, uniquely define the function δ_h . To determine the actual Φ , we first must solve a system of equations to determine $C = \frac{3}{8}$. Once C is determined, we solve for Φ on the interval $[0, 1]$ using equation using another system of equations. Once we have determined the value of Φ on the the interval $[-2, 2]$ using our system of equations, we let r be any real number,

$$\Phi(r) = \begin{cases} \frac{3-2|r|+\sqrt{1+4|r|-4|r|^2}}{8} & |r| \leq 1 \\ \frac{5-2|r|+\sqrt{-7+12|r|-4|r|^2}}{8} & 1 \leq |r| \leq 2 \\ 0 & 2 \leq |r| \end{cases} \quad (33)$$

To use the Immersed Boundary Method to model our system, we use the following:

1. Compute the elastic force density of the Lagrangian mesh,

$$\mathbf{F}(q, t) = F[\mathbf{X}(\cdot, t); q, t]$$

2. Spread the elastic force density from the Lagrangian mesh to the Eulerian grid,

$$\mathbf{f} = \int_{\Gamma} \mathbf{F}(q, t) \delta(\mathbf{x} - \mathbf{X}(q, t)) dq$$

Table 1: Physical parameters

Parameter	Value
Ω	0.25 m
ρ	1000 kg/m ³
s	0.03 m
c	0.05 m
δ	0.001 m
ν	0.3
Amplitude	2.5e-3 Hz
μ	.001 Ns/m ³

Table 2: Grid spacing parameters

Parameter	Value
Ngrid	512;
dx	4.88E-4;
L	.05;
NS_L	205;
ds_L	2.45E-4;
W	.001;
NS_W	5;
ds_W	2.50E-4;

3. Numerically update the incompressible Navier-Stokes equations on the Eulerian grid,

$$\rho \left(\frac{\partial \mathbf{u}(\mathbf{x}, t)}{\partial t} + \mathbf{u}(\mathbf{x}, t) \cdot \nabla \mathbf{u}(\mathbf{x}, t) \right) = -\nabla p(\mathbf{x}, t) + \mu \Delta \mathbf{u}(\mathbf{x}, t) + \mathbf{f}(\mathbf{x}, t)$$

$$\nabla \cdot \mathbf{u} = 0$$

4. Update the mesh position by interpolating from the local fluid velocity,

$$\mathbf{U}(q, t) = \frac{\partial \mathbf{X}(q, t)}{\partial t} = \int_{\Omega} \mathbf{u}(\mathbf{x}, t) \delta(\mathbf{x} - \mathbf{X}(q, t)) d\mathbf{x}$$

We repeat these steps at every time step to simulate the interaction between a background flow and our elastic panel.

7 Heaving Flexible Panel in Fluid Model

Now that we have constructed our panel, background flow and system, we are ready to conduct our tests. Our physical parameters are listed in Table 1. Our grid spacing parameters necessary for use of the immersed boundary method at listed in Table 2. To compare thrust and effective flexibility, we will vary the flexural rigidity (by varying the value of our beam constant) of the panel, as well as the frequency that the panel is heaved

at, and we will measure thrust output at every time step. Panels will have k_b s of 1E-5, 1E-6, 1E-7, 1E-8. Within each beam stiffness category, the panels will be heaved at frequencies from 0.25 Hz to 2.0 Hz, in increments of 0.25 Hz. For this test, we will have panels of four different rigidities, each being heaved at eight different frequencies. k_s is a function of k_b and is proportionally smaller than k_b .

To compare thrust outputs for uniform and nonuniform stiffness panels, we use uniform panels of 1E-6, and 1E-7 stiffnesses and nonuniform panels composed of a combination of the same stiffnesses. One nonuniform panel is composed of one third 1E-6 stiffness starting from the leading edge, two thirds 1E-7 stiffness for the remainder of the beam while the other is two thirds 1E-6 stiffness starting from the leading edge. These panels will be heaved at a frequency 1.5 Hz, and thrust output and beam deflection data will be recorded. The thrust output will be used to investigate the difference in thrust output of panels with uniform and nonuniform stiffnesses while the deflection data will be used to perform beam mode analysis described in a previous section of the panels with uniform stiffnesses.

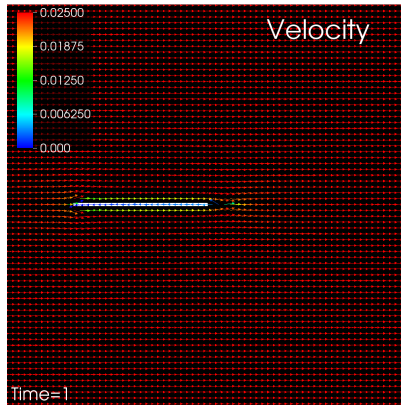
8 Results

8.1 Simulating Panel

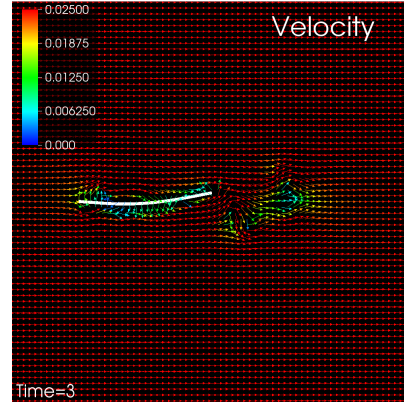
We successfully simulated a heaving panel in an incompressible flow. We apply a Butterworth filter in order to eliminate the high frequency signal. We also adjust for drag in our simulations by subtracting the thrust that is generated by a nonheaving panel in the same fluid. In Figure 10 we see the velocity vectors of the fluid at various time steps. In Subfigure 10a, we see the background flow changing at time 1 as soon as the panel begins to heave. This image best illustrates the no-slip boundary condition of the panel as the velocity immediately surrounding the beam is slower than the general background flow velocity. In Figure 10b, the panel has completed two cycles of heaving. The velocity of the fluid is affected by the forces of the panel. This interaction is modeled using the Immersed Boundary Method. In Subfigure 10c, the periodic heaving of the panel has generated similar patterns of velocity trailing the beam. As represented by the Immersed Boundary Method, the velocity of the entire fluid domain is affected by the movement of the panel. By looking at the sequence of pictures, we can see the velocity changing over time. This can represent the acceleration of the fluid surrounding a propulsor.

We relate the changes in velocity with the vortices in Figure 11. In Subfigure 11a the background flow has become established and the heaving motion has not begun. Therefore, there are no trailing concentrated vortices. The fluid that is flowing over the panel has a negative vorticity due to the no-slip boundary condition of the beam equation. The fluid vorticity directly below the panel is also positive based on the same condition. In Subfigure 11b, the panel has trailing vortices. However, the vortices are not significantly impacting one another. Looking at Subfigure 11c, after five periods of heaving motion, the trailing edge vortices are directly impacting each other causing consistent and concentrated core vortices in the wake of the panel. Overall, we can visualize how the vortices directly impact the fluid and the movement of the following vortex core.

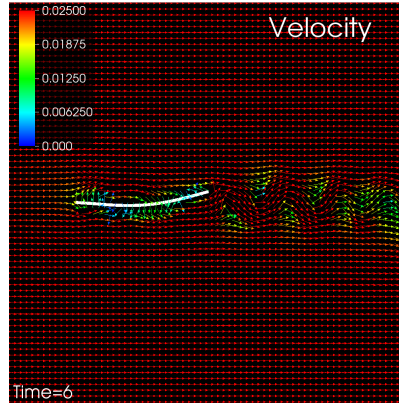
We see that there are initial vortices generated by the beam. After consistent heaving, the



(a) Background Flow Velocity at Time=1



(b) Background Flow Velocity at Time=3



(c) Background Flow Velocity at Time=6

Figure 10: k_b of $1\text{E-}6$ N/m heaved at a frequency of 1.0

Panels	Thrust Output (N)
Panel A	-0.002923364371063
Panel B	0.001595252938602
Panel C	0.001595252938362
Panel D	-0.004197654837758

Table 3

vortices generated by initial heaving begin to affect the subsequent vortices. Eventually the fluid forces created by the vortices hold the shredding vortices in a consistent shedding pattern.

We observe that three panels of different flexibilities heaved at the same frequency exhibit different vortex shedding patterns, both in quality and consistency. As shown in Figure 12, at time=6, the panel with beam stiffness of $k_b = 1E - 7$ had the most controlled stream of vortices in the wake of the beam, while the panel with beam stiffness of $k_b = 1E - 5$ had the least controlled stream of vortices.

In Figure 14, each line represents a different beam stiffness, and each asterisk represents a different frequency from 0.25 to 2.0 Hz with an interval of 0.25 Hz. We varying effective flexibility in order to see thrust dependency. At low frequencies ($\omega = [0.25 : 1]$), there seems to be an inverse relationship between effective flexibility and thrust. However, at frequencies greater than 1, we find that there does not seem to be a direct relationship between effective flexibility and thrust output. However, we have not connected effective flexibility to trailing edge amplitude or trailing edge amplitude to thrust output as in previous studies [8].

8.2 Uniform vs. Nonuniform Panels

We analyze the performance of panels with uniform and nonuniform stiffnesses. Performance is measured by the average thrust output of each panel at a frequency of 1.5 Hz. The panels were labeled A, B, C, and D, in order of proportion of beam stiffness $1E - 6$ to beam stiffness $1E - 7$. We define a panel as "flexible" if $k_b = 1E - 7$, and we label as panel as "stiff" if $k_b = 1E - 6$. Thus Panel A is flexible, Panel B is one-third stiff, two-thirds flexible, Panel C is two-thirds stiff, one-third flexible, and Panel D is stiff. Our thrust values were collected using data from our heaving panel simulation in IBAMR, where thrust was the force in the x-direction. Net thrust values were calculated as the force in the x-direction less the drag generated by the panel's structure. The drag was calculated using force data from a simulation of a static panel within an incompressible flow. The general trend of our analysis reveals that panels with non-uniform stiffness generate a higher thrust than that of panels with uniform stiffness. The two beams of non-uniform stiffness generated approximately the same amount of thrust. See Table 3 for thrust output per panel.

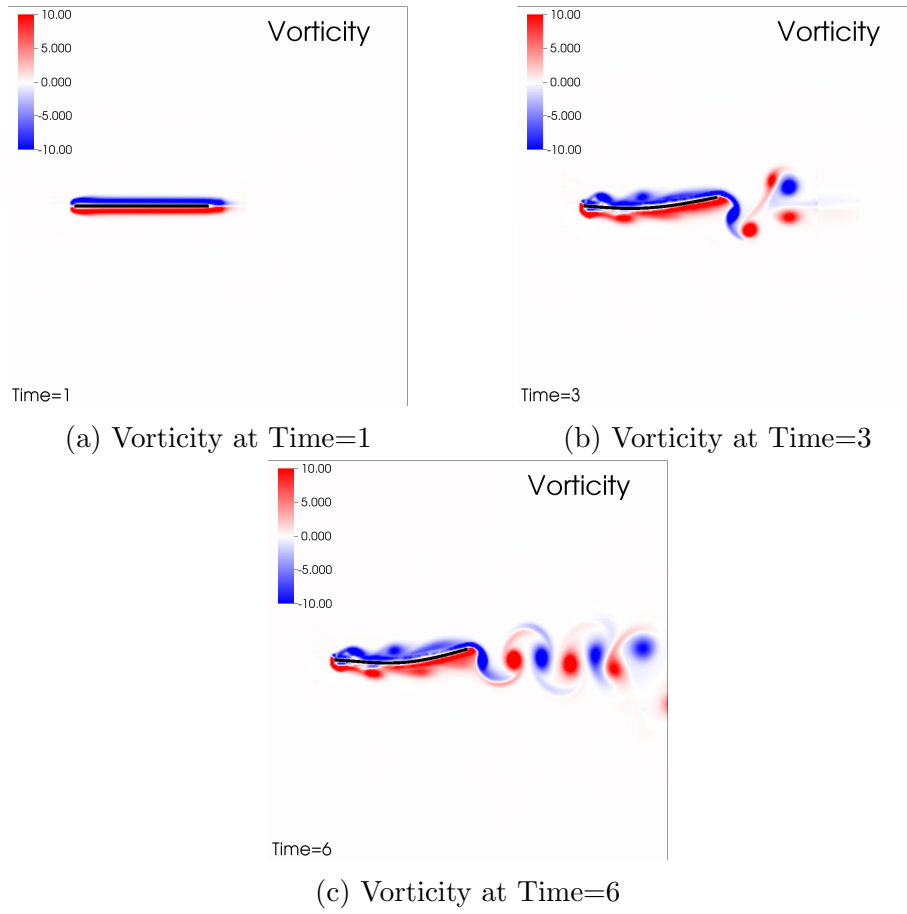


Figure 11: k_b of $1\text{E-}6$ N/m heaved at a frequency of 1.0

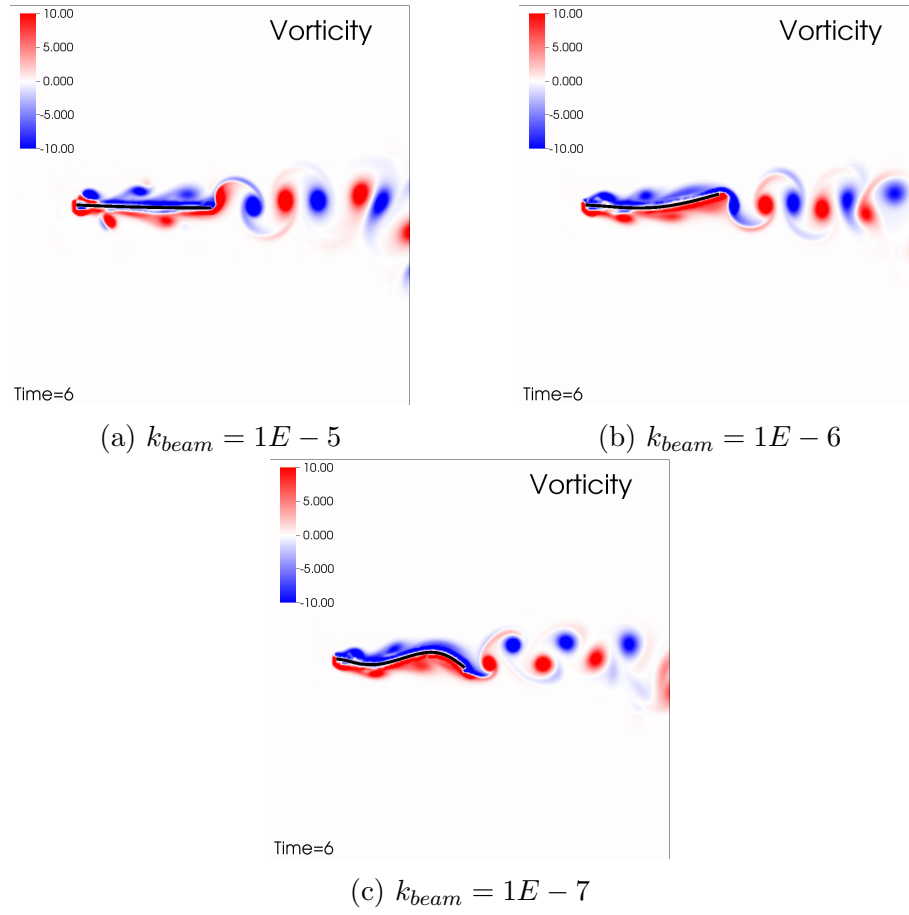


Figure 12: k_b of $1E-6$ N/m heaved at a frequency of 1.0

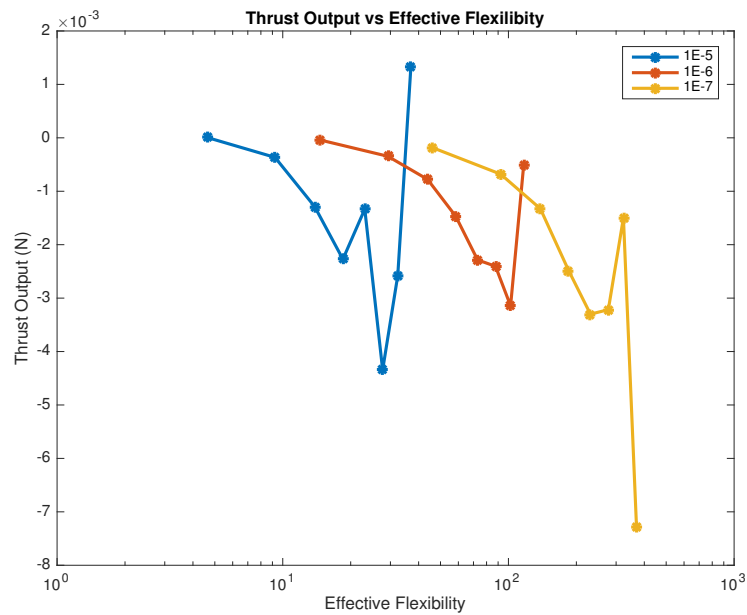


Figure 13: Thrust Versus Effective Flexibility for Various Beam Stiffnesses

8.3 Beam Mode Analysis

We perform the beam mode analysis for panels with uniform beam stiffnesses $k_b = 1E-6$ (stiff panel) and $k_b = 1E-7$ (flexible panel). The frequency that we heave the beams at is $\omega = 1.5$ Hz; this frequency value is chosen due to an interesting relationship that the beams shared when comparing their effective flexibility Π_i and their thrust when heaved at this frequency. The experimental deflection is generated using the panel's y-coordinate output from the IBAMR simulation. The y-coordinates of the heaving beam were output in relation to the y-coordinate of the leading edge. After v_{exp} was generated, the solution to the Euler-Bernoulli Beam Equation was used to decompose the transverse movement of our heaving panel into four different eigenmodes $\hat{\phi}_1, \hat{\phi}_2, \hat{\phi}_3, \hat{\phi}_4$. Recall that the sum of an infinite amount of eigenmodes would provide an exact model of our experimental deflection. Thus the shape of our modal approximation was close to the shape of the experimental deflection, but not exact; $v(x, t)$ would match v_{exp} more precisely if more values of k were included in the summation of $v(x, t)$.

We confirm this by plotting the deflection across the length of the beam, and analyzing the similarity between the modal approximation $v(x, t)$ and the simulated data v_{exp} , over time, for both beam stiffnesses. As expected, the modal contribution of the four eigenmodes closely approximated the simulation data for both beam stiffnesses.

The next part of analysis is investigating the dominance of each eigenmode throughout all cycles. We investigate the eigenmodes because dominant eigenmodes of the Euler-Bernoulli Beam Equation correspond to the effective flexibility, Π_i .

We plot the modal contributions $\hat{\phi}_i C_i$ over time, for each $i = 1, 2, 3, 4$. The number of modal contributions relies on the number of solutions k that we use to decompose the beam equation. In our panel with $k_b = 1E-6$, ϕ_1 is the dominant eigenmode over time. However, decreasing the panel stiffness to $k_b = 1E-7$, we observe that ϕ_3 is the dominant eigenmode over time. We expect that there is a localized thrust increase in relation to these dominant eigenmode values.

9 Conclusions

In summary, based on our data we find that nonuniform panels output a greater thrust than uniform panels of the same stiffnesses. By performing a beam-mode analysis on our panels with beam stiffnesses of k_b of $1E-6$ and $1E-7$, we link effective flexibility to beam modes. From there, there exists a relationship between beam modes and trailing edge amplitude. Previous studies have shown that trailing edge amplitude relates to local maximas of thrust output [8]. In continuing our work, we shall expand our parameter space to incorporate a more flexible panel and vary the heaving frequency by shorter intervals. By expanding our parameters, we will continue to investigate the relationship between effective flexibility, thrust, and beam stiffness. Furthermore, we shall investigate panels with non-uniform stiffnesses using an adapted beam mode analysis method to attempt to determine a more specific

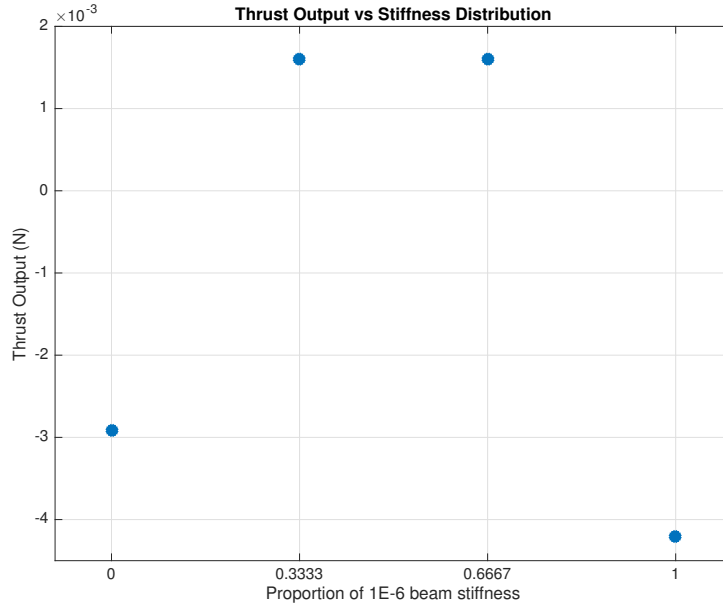
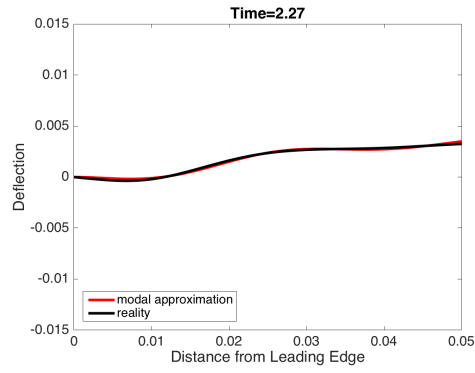
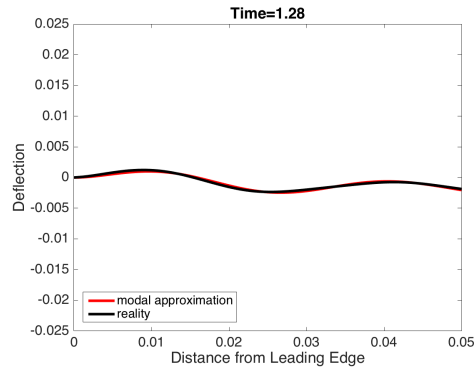


Figure 14: Thrust Output for various uniform and nonuniform stiffnesses



(a) k_b of $1\text{E-}6$ N/m



(b) k_b of $1\text{E-}7$ N/m

Figure 15: $\omega = 1.5$

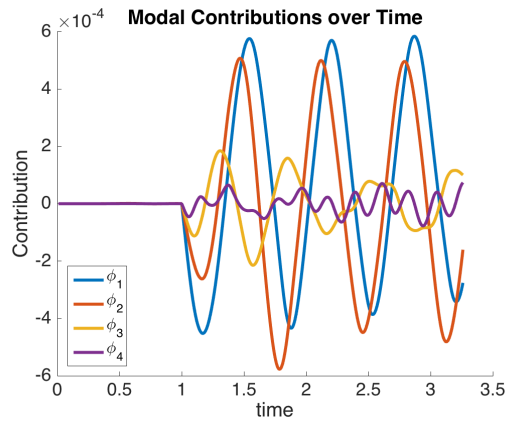
relationship between panels of non-uniform stiffnesses and thrust output maximas.

Acknowledgements

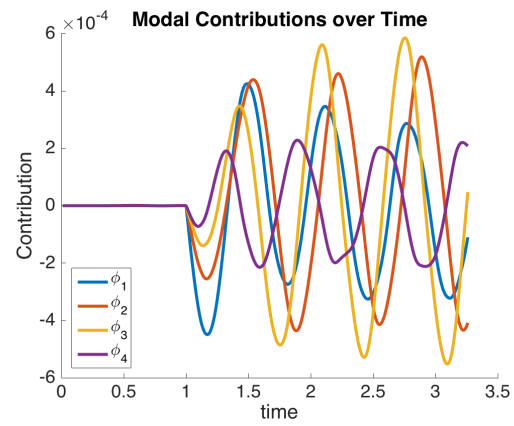
We would like to thank Dr. Ricardo Cortez, Dr. Lisa Fauci, and Dr. Alex Hoover of Tulane University. This work was conducted at the Center for Computational Science at Tulane University and funded in part by National Science Foundation grant No. DMS-1043626 “EMSW21: RTG: Mathematical and Computational Biofluids.”

References

- [1] D. J. Acheson. *Elementary Fluid Dynamics*. Clarendon Press, Oxford, England, 1990.
- [2] R. Dillon and L. Fauci. An integrative model of internal axoneme mechanics and external fluid dynamics in ciliary beating. *J. Theor. Biol.*, 207:415–430, 2000.
- [3] Kelsey N. Lucas. Bending rules for animal propulsion. *Nature Communications*, 5:3293, 2014.
- [4] Kelsey N. Lucas. Effects of non-uniform stiffness on the swimming performance of a passively-flexing fish-like foil model. *IOP Science*, 10, 2015.
- [5] J. M. McDonough. Lectures in elementary fluid dynamics: Physics, mathematics, and applications. 2009.
- [6] Charles S. Peskin. The immersed boundary method. *Acta Numerica*, pages 479–571, 2002.
- [7] Charles S. Peskin and David M. McQueen. *Fluid dynamics of the heart and its valves*. Prentice-Hall, Englewood Cliffs, NJ, 1992.
- [8] Daniel B. Quinn. Scaling the propulsive performance of heaving flexible panels. *Journal of Fluid Mechanics*, 738:250–267, 2013.
- [9] Jr. W. Weaver, S. P. Timoshenko, and D. H. Young. *Vibration Problems in Engineering*. Wiley-Interscience, New York, 1990.



(a) k_b of 1E-6



(b) k_b of 1E-7

Figure 16: Modal Contributions Over Time